# TESTING SPATIALLY FLEXIBLE BOTTOM BOUNDARY PARAMETER SCHEMES AND PRIORS FOR GEOTHERMAL RESERVOIR MODELS

Elvar K. Bjarkason[1], Oliver J. Maclaren[2], John P. O'Sullivan[2], Michael J. O'Sullivan[2], Anna Suzuki[1] and Ruanui Nicholson[2]

[1]Institute of Fluid Science, Tohoku University, Sendai, Japan

[2]Department of Engineering Science, The University of Auckland, Auckland 1142, New Zealand

e.bjarkason@tohoku.ac.jp ruanui.nicholson@aucklanduni.ac.nz

**Keywords:** *Geothermal model calibration, boundary conditions, uncertainty quantification, ensemble-based methods, parameterisation, reservoir modelling.*

## ABSTRACT

Geothermal reservoir models require suitable bottom boundary conditions to account for the influence of deep geothermal energy sources. When applying mass- and heat-flux boundary conditions to a model, it is standard practice to assign mass upflows to fixed locations on the bottom boundary. That is, during automatic model calibration, each boundary mass-flux region does not change its position, area, or shape. This rigidity in boundary source locations may limit 1) how well automatic calibration methods can match field data, and 2) how well model uncertainty is quantified. Here we consider more flexible parameterisation schemes and parameter priors to address those issues. The parameterisation schemes we use are based on sampling from multivariate Gaussian prior parameter distributions and applying thresholding to generate boundary regions that act as sources of geothermal fluid. Unlike the standard approach, the schemes proposed here allow upflow regions to appear on parts of the bottom boundary in keeping with field observations. This spatial flexibility not only enables upflow regions to appear or grow in order to better match observations but, in the context of uncertainty quantification, also allows the existence, geometry, and extent of upflow regions to vary between posterior sampled models. We demonstrate our parameterisation methods by applying them to uncertainty quantification of synthetic test models, including a model which is based on the Montserrat geothermal field.

## 1. INTRODUCTION

Previously, in (Nicholson et al., 2020), we proposed flexible parameterisation schemes for use in calibration and uncertainty quantification of geothermal reservoir models. These parameter schemes appear promising for describing variability in physical parameters governing flow of geothermal fluid through porous and fractured subsurface rock formations, such as formation permeability, porosity, and thermal conductivity. Other notable parameters include those that are used to assign heat- and mass-flux bottom boundary conditions. Such boundary conditions are used to introduce geothermal energy originating from deep sources into a geothermal model domain (Figure 1).

Our previous work focused on simple, efficient methods for generating parameter fields, but did not directly consider their use in solving inverse problems. In the current stage of our work, we thus consider testing and verifying the parameter schemes we proposed in (Nicholson et al., 2020) as part of an inverse problem or uncertainty quantification workflow. We focus on a parameterisation scheme which can be applied to assign mass-flux boundary conditions, as these parameters are the main driving force of transport of geothermal fluid in models describing geothermal systems, and its use in an iterative ensemble smoother method (Emerick and Reynolds, 2013; Emerick, 2016) described below (see also Bjarkason et al., 2021).

Traditional geothermal model calibration procedures assign and maintain mass-flux regions at fixed locations. Thus, traditional parameter schemes may not be flexible enough since the fixed regions may not include upflow regions that exist in the field, and may, therefore, result in parameter estimates and models which reflect model uncertainty inadequately. In contrast to the rigid traditional approach, the approach considered here builds on our work in (Nicholson et al., 2020) and allows mass-fluxes that are consistent with field data to adaptively appear in regions of interest. As a result, we expect that this flexible scheme can provide more realistic and more reliable models. Here we present results of synthetic uncertainty quantification experiments, which involve estimating bottom boundary flux terms. One of the test problems considers a natural-state model, which is based on the Montserrat geothermal field. For the Montserrat test problem, we determine the reliability of estimated mass-fluxes and the resulting model predictions by comparing predicted values with those of a synthetic reference truth.

## 2. METHODOLOGY

### 2.1 Forward problem: natural state of a convective geothermal reservoir

As a realistic test problem, we consider a natural-state geothermal model based on the Montserrat geothermal field (Lehuger et al., 2018; van den Heuvel et al., 2020). The geothermal reservoir simulator we applied in this study is AUTOUGH2 (Yeh et al., 2012), which is the University of Auckland's version of TOUGH2 (Pruess et al., 1999; Pruess, 2004). The steady-state mass and energy transport equations we aim to solve when running an AUTOUGH2 model to natural state can be represented as

$$\int_{\Omega_i} \boldsymbol{F}_\kappa \cdot \boldsymbol{n} \, \mathrm{d}\Omega = \int_{V_i} q_\kappa \, \mathrm{d}V \, . \qquad (1)$$

Here $\kappa$ denotes a transported quantity, such as energy, water, or air. The right side of Equation (1) accounts for sources within a control volume $V_i$, where $q_\kappa$ is the volumetric source rate of quantity $\kappa$. The source terms are balanced against the fluxes of the


ISSN 2703-4275

corresponding quantity $\boldsymbol{F}_\kappa$ passing through the surface $\Omega_i$ which bounds the volume. The term $\boldsymbol{n}$ denotes a unit normal vector for the bounding surface. The mass fluxes are assumed to be governed by Darcy's law, while the transported energy is governed by both the energy content of the transported mass and thermal conduction. For more details on TOUGH2 and geothermal reservoir modelling see, for instance, (Pruess et al., 1999; Pruess, 2004; O'Sullivan et al., 2001; O'Sullivan and O'Sullivan, 2016b).

A natural-state simulation of a high-temperature, convective geothermal system is carried out by running a transient simulation up to a large simulation time at which point, all being well, the simulator achieves a suitable approximation to the solution of the steady-state problem (1). When applying an automated inversion algorithm to match a natural-state geothermal model to data, it is important that the simulations achieve a large simulation time to ensure a robust inversion (Bjarkason et al., 2019a). Here we chose a maximum simulation time of $10^{15}$ s and assumed that the final state of simulations which achieved that target time represented reliable natural-state solutions for the assigned model and parameters. However, as discussed in (Bjarkason et al., 2019b), we note that a geothermal natural-state simulation is not guaranteed to be unique for a chosen combination of model and model parameters.

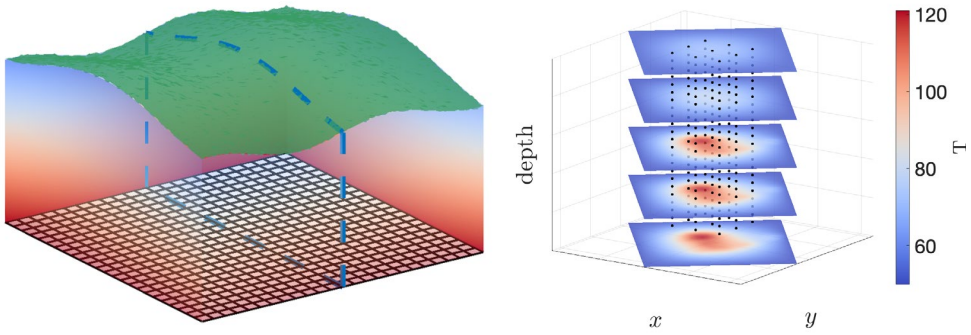


**Figure 1: (Left) Sketch of a model domain used to describe a geothermal system. The top of the model follows the local topography. Deep sources, which supply the system with hot geothermal fluid, are defined on the bottom boundary. (Right) Horizontal slices showing natural-state model temperatures [°C] and locations of temperature observations in wells (black circles).**

### 2.2 A more manageable forward problem: thermal conduction

The geothermal reservoir simulator needs to navigate various fluid-phase transitions in both space and time when solving a natural-state problem for a high-temperature geothermal system. As a result, geothermal reservoir simulations are notoriously time-consuming. Since such geothermal simulations are computationally demanding, in our preliminary testing of our proposed parameterisation schemes we consider using a substantially easier (conceptually and computationally) thermal conduction problem. The forward simulation equation we consider is the three-dimensional steady-state heat conduction equation:

$$\nabla \cdot (K \nabla T) = 0 \,, \tag{2}$$

with a known homogeneous top boundary flux and prescribed lateral temperatures. Here $T$ denotes the formation temperature and $K$ is the thermal diffusivity of the formation. We use this simple steady-state conductive model as a computationally cheap alternative to modelling steady natural-state conditions of a high-enthalpy geothermal system. This allows us to quickly examine the qualities of potential templates for assigning mass-flux boundary conditions before trialling those schemes in a geothermal reservoir model.

Note that we are not interested in the exact physical meaning of the forward problem defined by Equation (2) and its parameters. Instead, we simply want to use it as a sandbox for testing our boundary parameterisation schemes. Specifically, we use (2) for preliminary testing of how well our parameterisation schemes can reproduce expected patterns in parameters of interest, after calibration to data.

### 2.3 Boundary mass-flux parameters

Deep upflows of geothermal fluid and energy are accounted for in a geothermal reservoir model by assigning suitable sources of mass and heat to the base of the model (Figure 1). Here we assume a modelling convention where mass and heat are introduced into the model through the bottom boundary by assigning mass and heat fluxes across the boundary. For further information on bottom boundary conditions used in geothermal modelling see, for example, (O'Sullivan et al., 2001; O'Sullivan and O'Sullivan, 2016a).

In the parameterisation tests presented in this paper, we focus our attention on mass-flux boundary conditions. Note, that when solving the simple heat conduction forward problem we use heat-flux boundary conditions along with Equation (2) as a surrogate for using the mass-flux boundary conditions which are applied when modelling a convective geothermal model.

Example distributions used for mass-flux boundary conditions for state-of-the-art geothermal models are illustrated in Figures 2 and 3. The leftmost image in the third row of Figure 2 depicts mass-flux regions used to account for upflow of hot mass in a model used to describe the Wairakei (New Zealand) geothermal system (Yeh et al., 2016). Note that boundary flux values shown in Figure 2 for the Wairakei-based model were scaled to range between zero and one; nevertheless, the key characteristics of the upflow regions are in line with those used for the Wairakei models considered in (Yeh et al., 2016; Bjarkason et al., 2019b). Figure 3 illustrates mass upflow regions in a model which was recently used to describe a geothermal field located on Montserrat (Caribbean) (van den Heuvel et al., 2020). As depicted, the boundaries of both models have a small number of subregions where the mass flux is positive. The remaining regions of the boundary have no mass fluxes associated with them. The Montserrat model has narrow, linear mass-flux


ISSN 2703-4275

regions which represent upward flow of hot geothermal fluid along faults or fault zones (Figure 3). The small upflow zone which only involves a single boundary block is in a location which corresponds to the location of a hot geothermal pond on Montserrat (van den Heuvel et al., 2020; Ryan et al., 2013). The Wairakei model also has some decidedly linear or fault-like mass-flux regions (Figure 2). However, most of the upflow is over expansive regions near the centre of the bottom boundary. These examples showcase mass-flux features which expert modellers think reflect features in geothermal systems. In this work, we consider adaptively estimating such boundary flux regions.

As proposed in (Nicholson et al., 2020), we consider applying multivariate Gaussian prior parameter distributions along with level-sets (truncation) to generate prior parameter samples for boundary fluxes. We apply Gaussian priors which promote smoothness and apply truncation to generate distinct subregions of upward mass-fluxes. For the examples presented here, we draw flux parameters from a Gaussian prior parameter distribution which has zero mean. The covariance $C(x-x', y-y')$ between two fluxes located at points $(x, y)$ and $(x', y')$ on the horizontal bottom boundary, is of the following form:

$$C(x-x', y-y') = \sigma_{xy}^2 \cdot \exp\left(-\frac{(x-x')^2}{s_x^2} - \frac{(y-y')^2}{s_y^2}\right) + \sigma_d^2 \cdot \delta(x-x')\delta(y-y') \,, \tag{3}$$

where $\delta(\cdot)$ is the Kronecker delta function. The marginal prior variance is then $\sigma_{xy}^2 + \sigma_d^2$ while the correlation length-scales along the $x$- and $y$- directions are given by $s_x$ and $s_y$, respectively. The $\sigma_d^2$ term appears on the diagonal of the resulting prior covariance matrix and can be used to condition the covariance matrix. It is worth noting that various other covariance functions can be used (Rasmussen and Williams, 2006). To suppress the appearance of negative mass-flux regions, we truncate negative flux values to zero. Applying this approach generates prior samples of fluxes that look like the example shown in the top left image in Figure 2. That example has two distinct upflow regions which are reminiscent of the large upflow regions appearing in the Wairakei model (Figure 2). Note that prior samples generated with the above prior are expected to result in prior samples where about half of the bottom boundary is covered by positive mass-flux regions. To reduce the prevalence of upflow regions, the prior mean can be reduced. Furthermore, the appearance of upflows can be suppressed or encouraged in certain regions, for example, by allowing the variance to vary with location (Nicholson et al., 2020), while the correlation length-scale can likewise be varied to increase the number of individual upflow zones in certain regions. However, those options were not considered in the present work.

Using this type of parameter prior we can allow the boundary mass flux of each boundary block to be an estimated parameter. Thus, we do not have to restrict ourselves to assuming that upflows can only appear within fixed regions of the bottom boundary. Instead, the spatial extent of boundary mass-flux regions can be adjusted along with their strengths to match observations. Our expectation is that this type of prior could work well for estimating upflow-regions similar to the larger regions present in the Wairakei model (Figure 2). On the other hand, samples from the above prior are not consistent with the narrow flux features in the Montserrat model. We leave it to future work to explore ways of generating samples consistent with such narrow fault-like features. For this preliminary analysis of the Montserrat model, we assume that the permeability structure is known and consider limiting mass flows from the boundary to permeable fault structures. That is, we truncate the boundary mass fluxes to zero for boundary blocks whose permeability is below a chosen threshold. This scheme is physically reasonable since we can expect mass fluxes associated with impermeable formations to be small. Furthermore, we expect that the numerical model may experience difficulties in converging to a natural-state solution when boundary mass fluxes are carelessly placed in impermeable formations. From a practical point of view, it may, therefore, be useful to avoid introducing boundary mass fluxes into impermeable model blocks. Accordingly, the problem of how to generate narrow upflow zones which correlate with locations of faults is, in essence, related to the problem of how to choose priors for permeable fault structures.

### 2.4 Iterative ensemble smoother: ES-MDA

As discussed above, we target using our parameterisation schemes along with iterative ensemble smoothers to estimate geothermal model uncertainty. The results presented here were found using an iterative form of the ensemble smoother called the ensemble smoother with multiple data assimilation (Emerick and Reynolds, 2013; Emerick, 2016) or ES-MDA for short. ES-MDA is initialized by sampling $N_e$ model parameter combinations from a prior parameter distribution. In the notation used here, $\boldsymbol{m}_j^0$ denotes the $j$th vector of $N_m$ model parameters sampled from the prior parameter distribution. The ES-MDA method iteratively converts the ensemble of prior samples to $N_e$ posterior parameter samples, which can be used to estimate the model uncertainty given some data $\boldsymbol{d}_{\text{obs}}$. In our case, the data vector includes $N_d$ natural-state temperature observations from wells (Figure 1).

The ES-MDA procedure applies $N_a$ iterations or assimilation steps. Each ensemble member is updated at the ($k$+1)th assimilation step by the following update rule:

$$\boldsymbol{m}_j^{k+1} = \boldsymbol{m}_j^k + \boldsymbol{C}_{\text{md}}^k\left[\boldsymbol{C}_{\text{dd}}^k + \alpha_{k+1}\boldsymbol{C}_{\text{e}}\right]^{-1}\left(\boldsymbol{d}_{\text{obs}} + \boldsymbol{e}_j^k - \boldsymbol{d}\left(\boldsymbol{m}_j^k\right)\right). \tag{4}$$

Here $\boldsymbol{C}_{\text{md}}^k$ is an empirically estimated $N_m \times N_d$ cross-covariance matrix which quantifies the relationship between the ensemble of model parameters $\boldsymbol{m}_j^k$ and the corresponding ensemble of simulated observations $\boldsymbol{d}\left(\boldsymbol{m}_j^k\right)$. Similarly, $\boldsymbol{C}_{\text{dd}}^k$ is an $N_d \times N_d$ auto-covariance matrix for the simulated observations. The ensemble estimated covariance matrices are given by

$$\boldsymbol{C}_{\text{md}}^k = \frac{1}{N_e-1}\sum_{j=1}^{N_e}\left[\boldsymbol{m}_j^k - \bar{\boldsymbol{m}}^k\right]\left[\boldsymbol{d}(\boldsymbol{m}_j^k) - \bar{\boldsymbol{d}}^k\right]^T \quad \text{and} \quad \boldsymbol{C}_{\text{dd}}^k = \frac{1}{N_e-1}\sum_{j=1}^{N_e}\left[\boldsymbol{d}(\boldsymbol{m}_j^k) - \bar{\boldsymbol{d}}^k\right]\left[\boldsymbol{d}(\boldsymbol{m}_j^k) - \bar{\boldsymbol{d}}^k\right]^T. \tag{5}$$

The ensemble averages appearing in (5) are given by

$$\bar{\boldsymbol{m}}^k = \frac{1}{N_e}\sum_{j=1}^{N_e}\boldsymbol{m}_j^k \quad \text{and} \quad \bar{\boldsymbol{d}}^k = \frac{1}{N_e}\sum_{j=1}^{N_e}\boldsymbol{d}(\boldsymbol{m}_j^k)\,. \tag{6}$$


ISSN 2703-4275

In addition to the variability in the models sampled from the prior, ensemble variability is further promoted by the addition of stochastic observation noise in the update Equation (4). For every assimilation step and ensemble member, additional noise $\boldsymbol{e}_j^k$ is resampled from a normal distribution $\mathcal{N}(\mathbf{0}, \alpha_{k+1}\boldsymbol{C}_\mathrm{e})$, where $\alpha_{k+1}\boldsymbol{C}_\mathrm{e}$ is the covariance matrix for the noise. Note that $\boldsymbol{C}_\mathrm{e}$ is the assumed covariance matrix for the observation noise of the original observations $\boldsymbol{d}_\mathrm{obs}$ and $\alpha_{k+1}$ is an inflation factor. The ES-MDA inflation factors should satisfy the following condition (Emerick and Reynolds, 2013):

$$\sum_{k=1}^{N_a} \frac{1}{\alpha_k} = 1 \,. \tag{7}$$

For our experiments, we set the number of ES-MDA iterations to 10 and we used a geometrically decreasing sequence of inflation factors based on a scheme presented in (Emerick, 2019). The chosen inflation factors are given by

$$\alpha_k = \gamma^{k-1}\alpha_1 = \gamma^{k-N_a}\alpha_{N_a} \,, \tag{8}$$

with $\alpha_{N_a} = 1.5$ and $\gamma = 0.3333$.

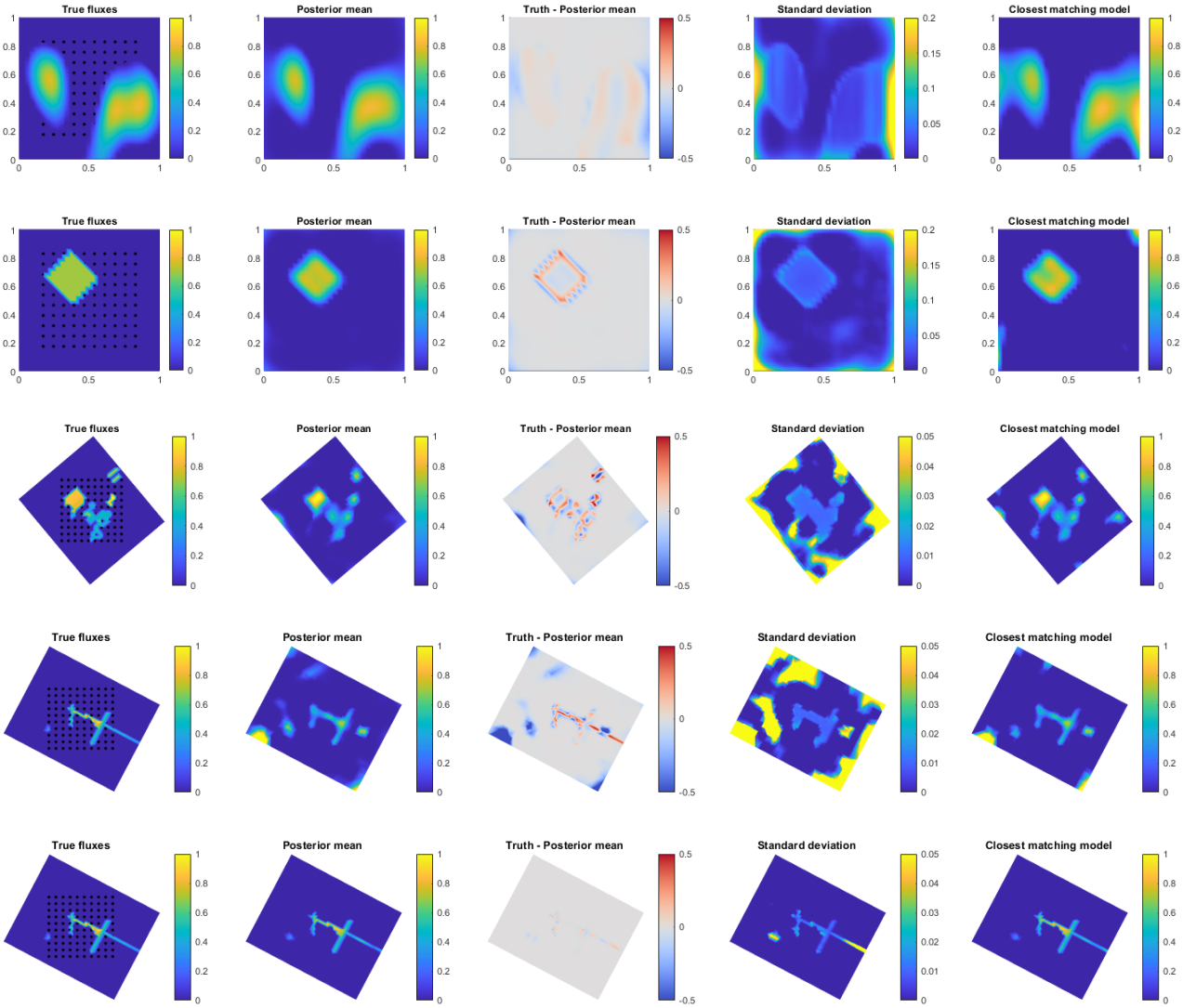


**Figure 2: Results from five test problems which consider estimating bottom boundary fluxes in simple thermal conduction models. (Top row) A case where the reference true fluxes are drawn from the prior distribution used for the uncertainty quantification. (Second row) Reference truth has a single square region of positive flux. (Third row) Reference boundary flux distribution based on a model describing the Wairakei geothermal field. (Last two rows) Reference boundary flux distribution based on a model describing the Montserrat geothermal field. The estimates in the last row were generated by restricting upflows to locations associated with permeable faults. The results in the row above did not apply prior knowledge of fault locations. For all test cases, the plots show the reference truth, the estimated posterior mean, the difference between the true fluxes and the posterior mean, the standard deviation of the posterior flux samples, and the posterior sample which gave the closest match to the observations. The black circles shown in the leftmost images indicate the locations of observation wells, which form a 10×10 grid.**

## 3. RESULTS

Here we present results for both the simple, steady-state heat conduction problem and the natural-state geothermal problem.

### 3.1 Tests using simple conductive models

As preliminary tests, we consider four different synthetic examples which apply the computationally cheap forward problem described in Section 2.2. For the first two examples, the true boundary fluxes are completely fictional and have simple distributions (see the first two rows in Figure 2). In the third example, the true boundary flux regions (see the third row in Figure 2) are based on the estimated boundary flux regions of the Wairakei geothermal field (Yeh et al., 2016; Nicholson et al., 2020; Bjarkason et al., 2019b). The fourth example applies boundary flux regions used in a model of the Montserrat geothermal field (van den Heuvel et al., 2020). For each test case, we sampled an ensemble of $10^3$ boundary flux distributions using the prior scheme discussed in Section 2.3. After that, we used those prior samples along with well observations as inputs into the ES-MDA algorithm, which subsequently generated an ensemble of $10^3$ posterior estimates of the boundary fluxes. In these four test cases, we assumed that we had temperature observations down 100 wells, which form a 10×10 grid pattern as shown in Figure 2. Notice that, for all four test cases, we have scaled the true reference boundary fluxes so that they have values ranging between zero and one (Figure 2).

#### 3.1.1 Reference model that is consistent with the prior

The first test case, which is illustrated in the top row of Figure 2, has a reference true flux distribution that was sampled from the applied prior distribution. The prior parameters controlling the correlation length-scale were chosen as $s_x = 0.2$ and $s_y = 0.5$, which results in anisotropic flux regions. The parameters controlling the variance of prior samples were $\sigma_{xy}^2 = 0.5$ and $\sigma_d^2 = 10^{-6}$. Note that we do not report units for these values and the results shown in Figure 2 since we are only interested in relative values and how well the combination of the prior samples and ensemble smoother manage to estimate the flux distributions.

The reference model has two boundary upflow regions. Figure 2 compares the reference fluxes with the estimated posterior mean and the fluxes of the posterior sample which gave the closest matches to the well data (closest matching model). Those results and the errors in the mean flux estimates suggest that the ES-MDA algorithm performed as expected. As anticipated, the variability of the posterior samples is greatest towards the edges of the model as indicated by the standard deviations of the boundary fluxes. This is generally the case for all test cases (Figure 2); that is, the parameter uncertainties tend to increase away from the wells.

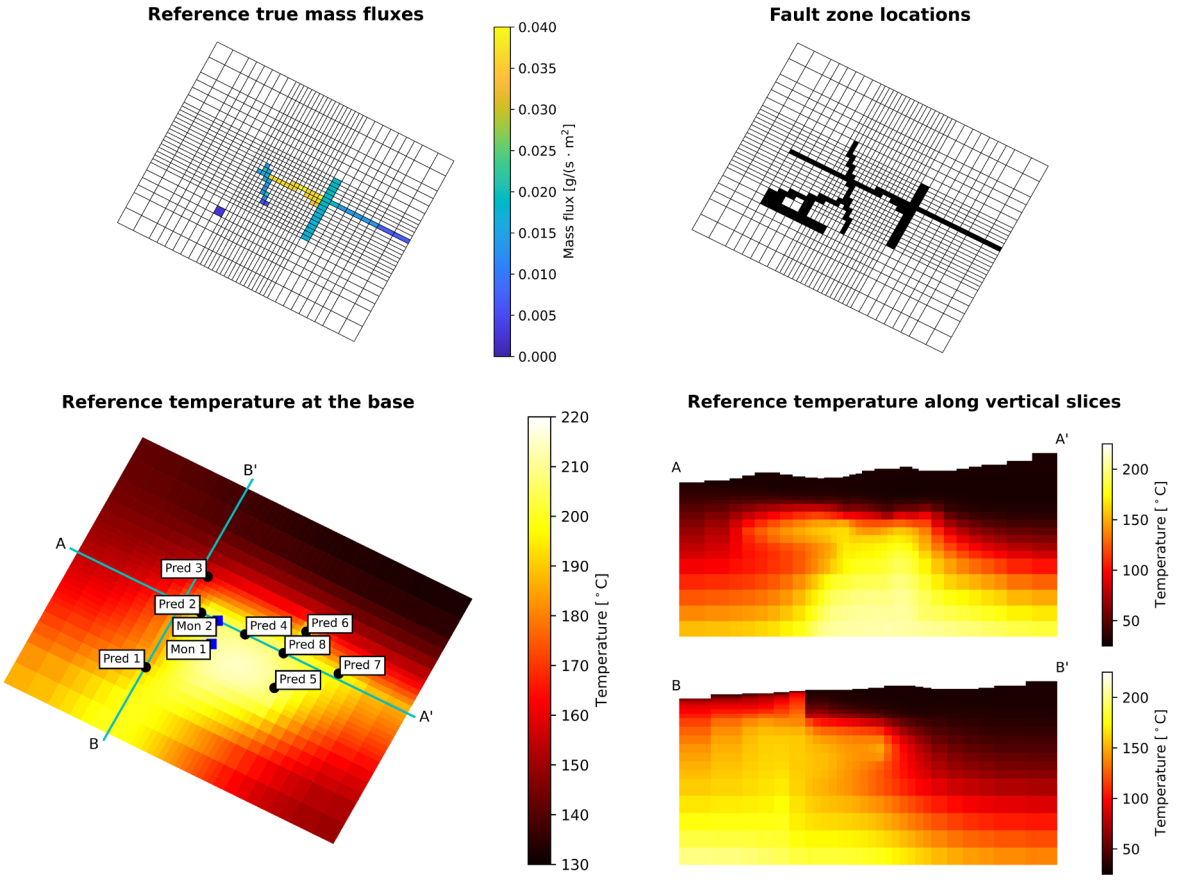


**Figure 3: (Top left) Applied bottom boundary mass-fluxes for a reference model based on the Montserrat geothermal field. (Top right) Locations of permeable faults on the bottom boundary. (Bottom left) Natural-state temperatures along the bottom boundary layer of the reference model. The markers indicate the locations of two observation wells (Mon 1 and Mon 2) as well as the locations of eight model columns or wells (Pred 1–8), which we use for model predictive checks. (Bottom right) Reference natural-state temperatures along vertical slices marked in the bottom left image.**

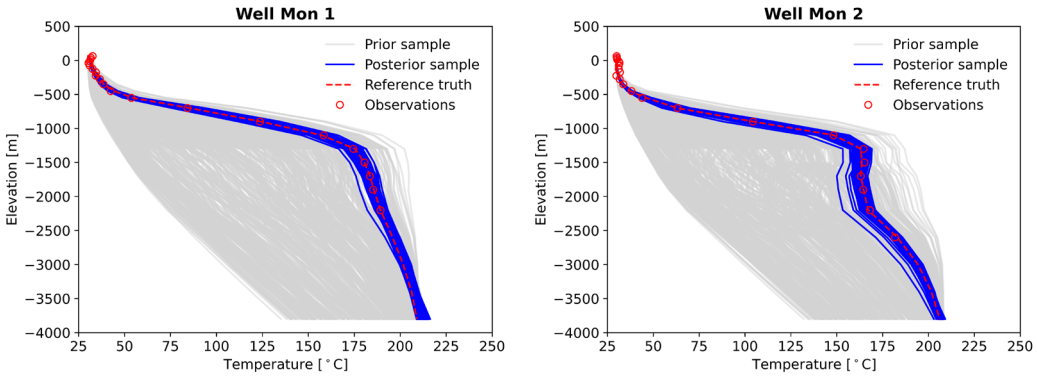


**Figure 4: Ensemble posterior model predictions compared with the natural-state temperature observations and reference model temperatures for observation wells Mon 1 and Mon 2. The prior predictions are also shown for reference.**

### 3.1.2 Reference square region

The second test looks at a case where the true fluxes are confined to a square region (second row in Figure 2). The prior covariance parameters were $s_x = 0.2$, $s_y = 0.2$, $\sigma_{xy}^2 = 2$ and $\sigma_d^2 = 10^{-6}$. For this case, the main characteristics of the true fluxes and location of the upflow zone are well reconstructed by the posterior mean and individual posterior samples, such as the closest matching model. However, some large errors are seen at, and near, the discontinuities in the true fluxes. This is to be expected as the prior density used (heavily) favours smooth flux distributions.

### 3.1.3 Flux regions based on a Wairakei model

The third test case has a reference model whose boundary flux distribution is based on the boundary mass fluxes of a model describing the Wairakei geothermal field. As mentioned above, we rescaled the reference fluxes. The parameters of the prior distribution we applied were $s_x = 5$ km, $s_y = 5$ km, $\sigma_{xy}^2 = 2$ and $\sigma_d^2 = 10^{-4}$. As the results in the third row of Figure 2 show, the posterior samples captured the main locations of the upflow regions. However, as was the case for the second test case, the posterior samples do not capture the discontinuities in the reference flux distribution since the prior density encourages smooth flux fields and the observations are imperfect/noisy. The estimated upflows associated with the location of the Ngatamariki geothermal field (located towards the northern edge of the model) have large uncertainties since they are on the edge of or outside the wellfield. Nevertheless, the posterior standard deviations suggest that we can be confident that most of the remaining areas close to the edges of the wellfield have little to no upflow on the bottom boundary.

### 3.1.4 Flux regions based on a Montserrat model

Figure 3 shows bottom boundary mass-fluxes from a model constructed to describe the Montserrat field. The leftmost figures in the last two rows of Figure 2 depict the corresponding scaled fluxes we chose as the reference boundary fluxes in the fourth test problem. We considered two types of prior models for estimating the boundary fluxes. In the first variant, we applied the same type of prior model as we presented for the previously discussed test cases. The parameters of the prior distribution we applied were $s_x = 1$ km, $s_y = 1$ km, $\sigma_{xy}^2 = 2$ and $\sigma_d^2 = 10^{-4}$. For the second variant, we used the same template for the prior but assumed additional knowledge of fault locations on the boundary and truncated the fluxes to zero outside the faults. The locations of the faults are shown in Figure 3. The results in Figure 2 show that both approaches managed to locate the upflow regions. For instance, both methods identified the small upflow region located towards the western end of the model, and as expected the posterior uncertainties are high for the upflow region located to the east of the wellfield. As the errors in the posterior mean show, the additional knowledge about the fault zones resulted in improved flux estimates, which is also an expected result.

### 3.2 An AUTOUGH2 model based on the Montserrat geothermal field

The natural-state model applied by van den Heuvel et al. (2020) to describe the Montserrat geothermal field is an air-water model. Here we look at estimating mass source terms appearing in a version of their Montserrat model. To expedite our testing, we converted the model considered by van den Heuvel et al. (2020) into a pure water EOS1 model and reduced the enthalpies of boundary source terms to 900 kJ/kg. This reduces the computational cost since it reduces the number of primary variables used for the simulations and supresses the appearance of two-phase domains. The reference bottom boundary fluxes are shown in Figure 3 along with the resulting temperatures for the bottom layer of the model and temperatures along two vertical slices. As observation wells, we used the locations of the two observation wells that exist in the Montserrat field called Mon 1 and Mon 2 (van den Heuvel et al., 2020). The locations of those wells are indicated by the blue squares in the bottom left image of Figure 3. Using the reference model, we generated natural-state temperature data down those wells by adding noise (sampled from a Gaussian distribution with zero mean and a standard deviation of 1°C) to the reference temperatures of model blocks intersected by the wells. The resulting synthetic observations are shown in Figure 4.

For this test case, we assume perfect knowledge of all model parameters apart from the values of the bottom boundary mass-fluxes associated with the fault zones shown in Figure 3. The parameters of the prior covariance matrix were chosen as $s_x = 1$ km, $s_y = 1$ km, $\sigma_{xy} = 2 \cdot 10^{-5}$ kg/(s m$^2$) and $\sigma_d = 2 \cdot 10^{-7}$ kg/(s m$^2$). The correlation length-scale seems reasonable since the model has a 7.5


ISSN 2703-4275

km by 6 km horizontal footprint. However, this is not necessarily the optimal choice of covariance parameters for this problem. Example prior flux samples are shown in Figure 5 along with the standard deviations of the ensemble of the 500 prior samples we used for this test case. As depicted, we restricted boundary upflows to the fault regions mapped in Figure 3.

Applying the ES-MDA method resulted in posterior samples which provided good matches to the observations in wells Mon 1 and Mon 2 (Figure 4). Figure 4 shows that the ensemble of posterior predictions provided reliable predictions of temperatures at locations directly below the deepest well observations. To analyse the predictive power of the posterior samples, we consider temperature predictions (see Figure 6) at locations of eight additional (fabricated) prediction wells that are shown in Figure 3. Those results indicate that the posterior predictions are reliable in the centre and eastern parts of the model. However, the posterior ensemble members tend to slightly overpredict the temperatures at locations west and north of the two observation wells (see results in Figure 6 for prediction wells 1–3). Nevertheless, the true temperature profiles for all the wells are contained within the ranges of the posterior predictions.

The sampled mass-fluxes appear to reveal why the overprediction tendency arose (see Figure 7). The posterior mean and fluxes of individual ensemble members indicate that the location of the strongest upflow region was estimated reasonably well. As we expected, the ensemble variability (see the standard deviations in Figure 7) was reduced most near the observation wells. Further away from those wells, the posterior standard deviation appears to be closer to that of the prior samples. We can also see that the posterior samples tend to be allocated a much larger influx of hot water towards the western corner of the model than is the case for the reference model, which only has a mass source in one boundary block in that region. It, therefore, appears to be the case that the applied prior is suboptimal in that region. That is, it tends to result in models with too much boundary upflow in that region.

## 4. CONCLUSION

In (Nicholson et al., 2020), we described simple, efficient methods for generating random parameter fields that can realistically represent the variability in physical parameters and boundary conditions in geothermal models. However, we did not consider their use in solving geothermal inverse problems and uncertainty quantification. Hence, as the next step in this process, in the present work, we considered using these random parameter fields as prior distributions along with iterative ensemble smoothers for solving geothermal inverse problems and carrying out uncertainty quantification. While real-world geothermal reservoir models involve simulating highly nonlinear heat and fluid transport through porous media, here we first considered an easier-to-run thermal diffusion (conduction) problem. This problem provided a simple sandbox for testing both our boundary flux parameterisation methods and their use in ensemble smoothing methods. We constructed and tested four thermal diffusion test cases, which included two models which had boundary flux distributions that were based on realistic values appearing in models used to describe the Wairakei and Montserrat geothermal fields. We found that our methods provided good estimates of boundary flux parameters and their associated uncertainties in our simple test problems.

In the second stage of our research, we tested our methods on a realistic and more computationally demanding natural-state geothermal reservoir model which is based on a model used to describe a geothermal system located in Montserrat. The results indicate that our schemes can provide reasonable estimates and error bounds for bottom boundary mass-fluxes appearing in a realistic geothermal model. Furthermore, the natural-state temperature predictions resulting from our uncertainty quantification workflow were, by and large, reliable. Nevertheless, it appears that more reliable predictions could be attained by reconsidering the applied prior parameter distribution. These preliminary results suggest that our proposed boundary flux parameterisation approach may be adaptable enough to represent features which are representative of mass fluxes present in geothermal systems.

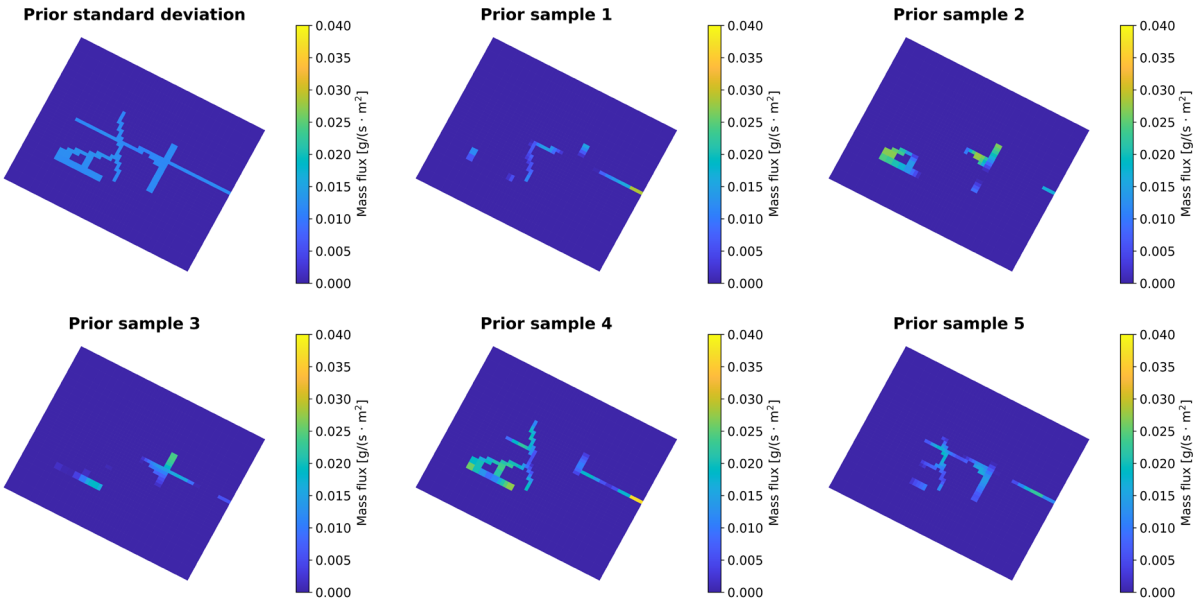


**Figure 5: Prior parameter standard deviation and example prior flux samples for the Montserrat test-case.**

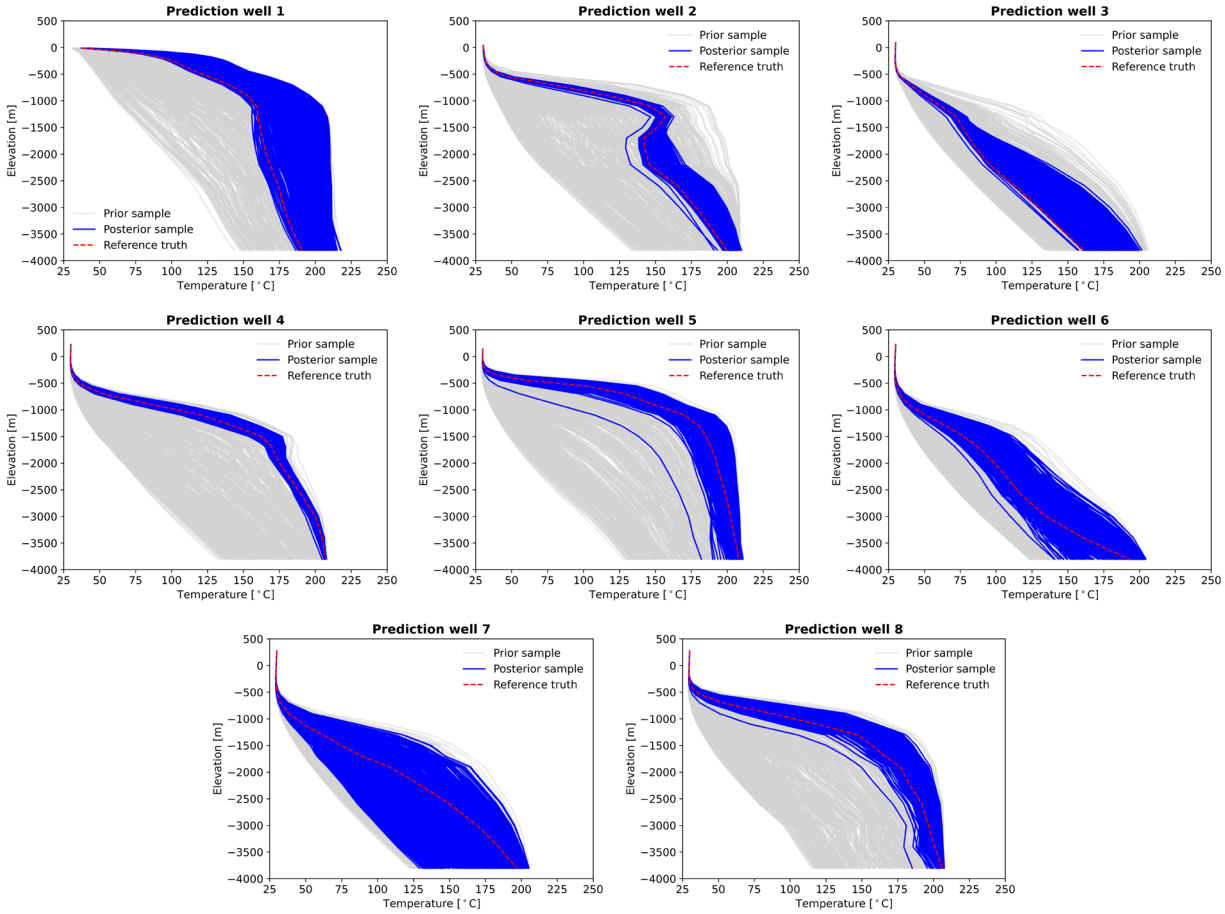


**Figure 6: Predicted natural-state temperatures down eight model columns, resulting from the ensemble of posterior samples, compared with the true reference temperatures. The prior predictions are also shown for reference. The locations of the model columns or wells are shown in Figure 3.**

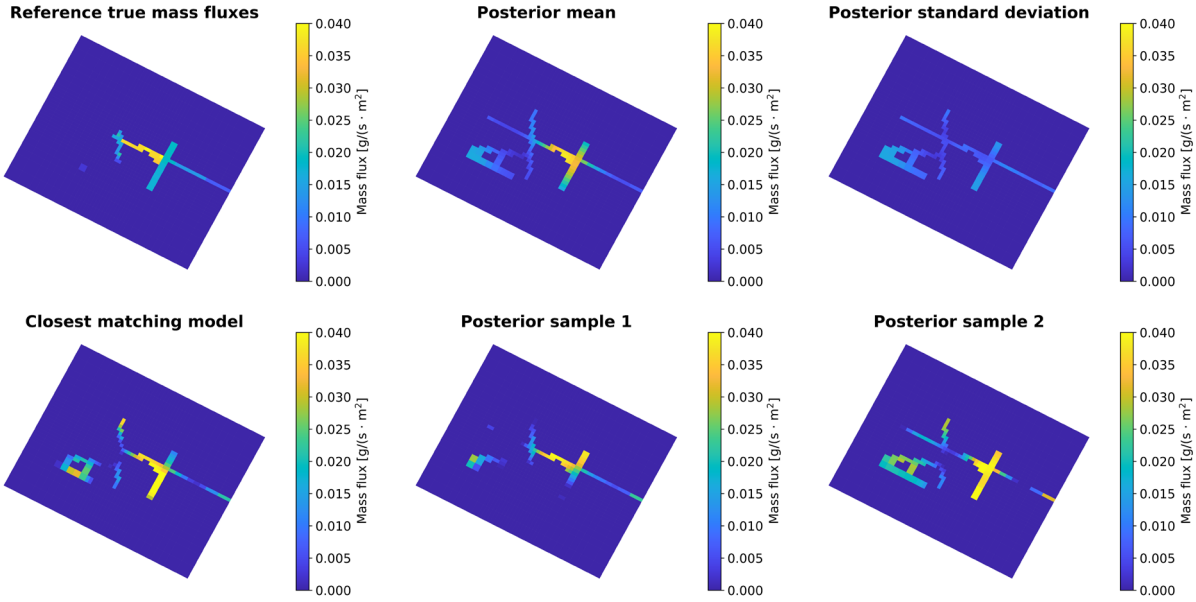


**Figure 7: Estimation results for the boundary mass-fluxes of the Montserrat model compared with the reference truth.**


ISSN 2703-4275

**ACKNOWLEDGEMENTS**

This work was carried out under the Collaborative Research Project of the Institute of Fluid Science, Tohoku University. This work was also partially supported by Landsvirkjun.

**REFERENCES**

Bjarkason, E.K., Maclaren, O.J., Nicholson, R., Yeh, A., O'Sullivan, M.J.: Uncertainty quantification of highly-parameterized geothermal reservoir models using ensemble-based methods. *Proc. World Geothermal Congress 2020+1,* Reykjavik, Iceland. (2021).

Bjarkason, E.K., O'Sullivan, J.P., Yeh, A., O'Sullivan, M.J.: Inverse modeling of the natural state of geothermal reservoirs using adjoint and direct methods. *Geothermics*. 78, 85–100. (2019a).

Bjarkason, E.K., Yeh, A., O'Sullivan, J.P., Croucher, A., O'Sullivan, M.J.: Non-uniqueness of geothermal natural-state simulations. *Proc. 41st New Zealand Geothermal Workshop,* Auckland, New Zealand. (2019b).

Emerick, A.A.: Analysis of the performance of ensemble-based assimilation of production and seismic data. *Journal of Petroleum Science and Engineering*. 139, 219–239. (2016).

Emerick, A.A.: Analysis of geometric selection of the data-error covariance inflation for ES-MDA. *Journal of Petroleum Science and Engineering*. 182, 106168. (2019).

Emerick, A.A. and Reynolds, A.C.: Ensemble smoother with multiple data assimilation. *Computers & Geosciences*. 55, 3–15. (2013).

Lehuger, U., O'Sullivan, M.J., O'Sullivan, J.P., Popineau, J., Ryan, G.A.: Computer modelling of Montserrat geothermal field. *Proc. 40th New Zealand Geothermal Workshop,* Wairakei, New Zealand. (2018).

Nicholson, R., Maclaren, O.J., O'Sullivan, J.P., O'Sullivan, M.J., Suzuki, A., Bjarkason, E.K: Representation of unknown parameters in geothermal model calibration. *Proc. 42nd New Zealand Geothermal Workshop*, Waitangi, New Zealand. (2020).

O'Sullivan, J.P. and O'Sullivan, M.J.: The effect of bottom boundary conditions on predictions of steam production from geothermal reservoir models. *Proc. 41st Workshop on Geothermal Reservoir Engineering,* Stanford University, Stanford, California. (2016a).

O'Sullivan, M.J. and O'Sullivan, J.P.: Reservoir modeling and simulation for geothermal resource characterization and evaluation. In *Geothermal Power Generation: Developments and Innovation*, ed. by R. DiPippo. 165–199. (2016b).

O'Sullivan, M.J., Pruess, K., Lippmann, M.J.: State of the art of geothermal reservoir simulation. *Geothermics*. 30(4), 395–429. (2001).

Pruess, K.: The TOUGH codes — a family of simulation tools for multiphase flow and transport processes in permeable media. *Vadose Zone Journal.* 3, 738–746. (2004).

Pruess, K., Oldenburg, C., Moridis, G.: *TOUGH2 User's Guide, version 2*, Lawrence Berkeley National Laboratory, Berkeley, California. (1999).

Rasmussen, C.E. and Williams, C.K.I.: *Gaussian processes for machine learning*. MIT Press. (2006).

Ryan, G.A., Peacock, J.R., Shalev, E., Rugis, J.: Montserrat geothermal system: A 3D conceptual model. *Geophysical Research Letters*. 40, 2038–2043. (2013).

van den Heuvel, M., Bremaud, M., O'Sullivan, M.J., O'Sullivan, J.P., Popineau, J., Guzman, S., Gravatt, M., Ryan, G.A.: An updated computer model of Montserrat geothermal field. *Proc. 42nd New Zealand Geothermal Workshop*, Waitangi, New Zealand. (2020).

Yeh, A., Croucher, A.E, O'Sullivan, M.J.: Recent developments in the AUTOUGH2 simulator. *Proc. TOUGH Symposium*, Lawrence Berkeley National Laboratory, Berkeley, California. (2012).

Yeh, A., O'Sullivan, M.J., Newson, J.A., Mannington, W.I.: Use of PEST for improving a computer model of Wairakei-Tauhara. *Proc. 38th New Zealand Geothermal Workshop*, Auckland, New Zealand. (2016).


ISSN 2703-4275